Modulating Nanoinhomogeneity at Electrode–Solid Electrolyte Interfaces for Dendrite-Proof Solid-State Batteries and Long-Life Memristors

Ziheng Lu,* Ziwei Yang, Cheng Li, Kai Wang, Jinlong Han, Peifei Tong, Guoxiao Li, Bairav Sabarish Vishnugopi, Partha P. Mukherjee, Chunlei Yang,* and Wenjie Li*

Dendrite penetration in ceramic lithium conductors severely constrains the development of solid-state batteries (SSBs) while its nanoscale origin remains unelucidated. An in situ nanoscopic electrochemical characterization technique is developed based on conductive-atomic force microscopy (c-AFM) to reveal the local dendrite growth kinetics. Using $Li_7La_3Zr_2O_{12}$ (LLZO) as a model system, significant local inhomogeneity is observed with a hundredfold decrease in the dendrite triggering bias at grain boundaries compared with that at grain interiors. The origin of the local weakening is assigned to the nanoscale variation of elastic modulus and lithium flux detouring. An ionic-conductive polymeric homogenizing layer is designed which achieves a high critical current density of 1.8 mA cm^{-2} and a low interfacial resistance of 14 Ω cm^2. Practical SSBs based on $LiFePO_4$ cathodes can be stably cycled over 300 times. Beyond this, highly reversible electrochemical dendrite healing in LLZO is discovered using the c-AFM electrode, based on which a model memristor with a high on/off ratio of $\approx 10^5$ is demonstrated for >200 cycles. This work not only provides a novel tool to investigate and design interfaces in SSBs but also offers opportunities for solid electrolytes beyond energy applications.

1. Introduction

Lithium-ion batteries (LIBs) since their commercialization have revolutionized the energy storage sector and are presently ubiquitous across portable electronics. However, recent advancement of the electric vehicle industry and grid-scale storage necessitates energy storage solutions beyond the current LIB technology with aggressive demands on safety,

Dr. Z. Lu, Z. Yang, C. Li, K. Wang, Dr. J. Han, P. Tong, G. Li, Dr. C. Yang, Dr. W. Li
Shenzhen Institutes of Advanced Technology
Chinese Academy of Sciences
Shenzhen 518055, P. R. China
E-mail: zh.lu1@siat.ac.cn; cl.yang@siat.ac.cn; wj.li@siat.ac.cn
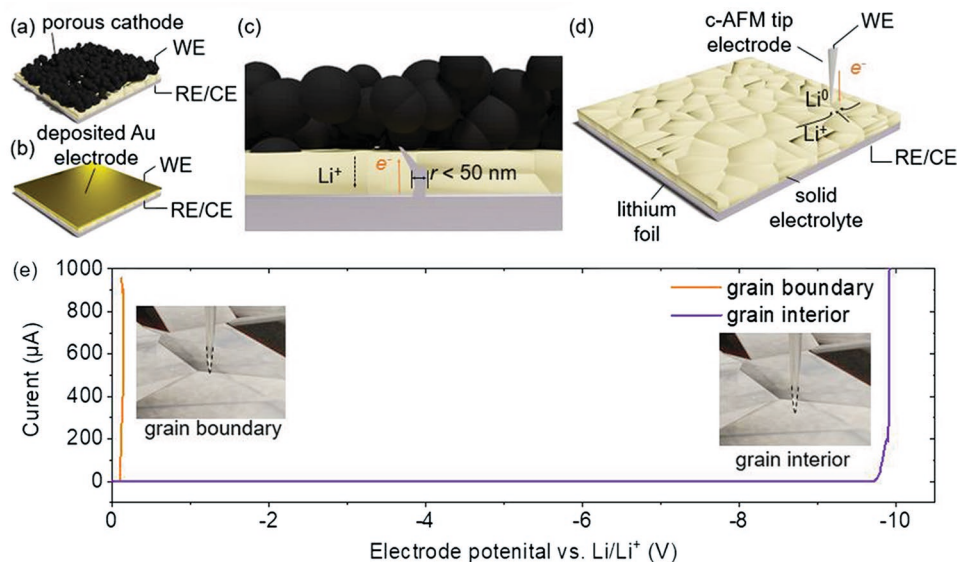B. S. Vishnugopi, Prof. P. P. Mukherjee
School of Mechanical Engineering
Purdue University
West Lafayette, IN 47907, USA

The ORCID identification number(s) for the author(s) of this article can be found under https://doi.org/10.1002/aenm.202003811.

DOI: 10.1002/aenm.202003811

price, and energy density.[1] Especially, in order to reach the target of 500 Wh kg^{-1}, replacing the current graphite anode with lithium metal has been considered critical.[2–5] Unfortunately, lithium (Li) metal is highly reactive and tends to electrodeposit into a dendritic morphology during cycling, which inevitably paves the way for cell failure. Extensive research efforts have been made in this regard and various strategies such as tuning the electrolyte composition,[6,7] coating Li metal with artificial layers,[8,9] designing porous current collectors,[10] and utilizing solid electrolytes (SEs)[11,12] have been proposed. Among these, replacing the conventional liquid electrolyte with mechanically stiff and Li⁺-conductive SEs has been regarded as one of the most promising solutions to address both the safety concerns and energy density limitations of LIBs. On the one hand, SEs are less flammable when compared to organic liquid electrolytes. On the other hand, due to their mechanical rigidity, SEs are expected to suppress the growth of uneven Li deposits.[13]

Among the SEs that have been discovered, ceramic oxides are one of the most promising families due to their high ionic conductivity, excellent fire redundancy, good mechanical strength, and the ease of fabrication in air. In particular, the lithium-stuffed garnet $Li_7La_3Zr_2O_{12}$ (LLZO) has garnered tremendous research attention since its discovery in 2007.[14] When properly doped, it displays a high ionic conductivity of over 10^3 S cm^{-1} and a Young's modulus of ≈ 150 GPa.[15,16] In addition, LLZO is one of the very few SEs that are chemically stable toward Li metal.[15,16] Owing to these attributes, LLZO has also been regarded as a promising candidate for employment in solid-state lithium-metal batteries (SSLMBs). In fact, one of the rationales behind the early investigation of LLZO, inferred from the linear elasticity model by Monroe and Newman,[17] was that its high shear modulus could suppress the growth of Li dendrites. However, this hypothesis has recently been challenged by several experimental findings that reveal the penetration of Li metal in LLZO and observation of internal short circuits at high current densities.[18] Since then, significant research efforts have been placed in understanding the

ADVANCED
SCIENCE NEWS
www.advancedsciencenews.com

ADVANCED
ENERGY
MATERIALS
www.advenergymat.de

Figure 1. Illustration of the macroscopic electrochemical measurement setups using a) porous cathodes and b) deposited Au electrodes. c) Illustration of the penetration of lithium filaments in a conventional macroscopic electrochemical measurement setup. d) Illustration of the nanoscale electrochemical measurement setup used in the current study where the c-AFM tip is used as the WE. e) Typical current response of applying a varying bias at grain boundaries and grain interiors using the c-AFM nanoelectrode.

mechanisms underlying the penetration behavior of Li metal. Hu et al. found that LLZO is poorly wetted by Li, even in its molten state. The poor interfacial contact leads to high local current densities and triggers local "hot spots" for Li to penetrate.[19,20] Sharafi and co-workers confirmed that the poor wettability is due to the surface contaminants such as LiOH and Li_2CO_3.[21] To quantify the capability of LLZO in blocking the dendrites, they further proposed the concept of critical current density (CCD) which is defined as the highest current density before a Li|LLZO|Li cell shorts.[22] Usually, for an LLZO pellet with untreated surface, the CCD does not exceed 0.2 mA cm^{-2}. This value is significantly lower than the 2 mA cm^{-2} threshold needed for practical applications. Apart from the contact issues, local inhomogeneity has also been identified as a source of instability for Li deposition. Importantly, the grain boundary is deemed to be a preferential nucleation site due to its high electron conductivity,[23] low elastic modulus,[24] and the low fracture toughness.[25–27] Recently, Porz et al. proposed a Griffith-like crack extension model where lithium metal infiltrates into the electrolytes through surface defects.[27] Considering the fundamental difference between the Li penetration in ceramic SEs and its dendritic-like growth in liquid electrolytes, we will use the term "filament" instead of "dendrite" throughout the article. In literature, various strategies have been proposed to enhance the stability of Li|LLZO interfaces and improve the CCD values, including physical/chemical treatment of the interfaces to enhance the interface contact,[19,20] designing composite anodes to modify its interactions with LLZO,[28,29] and modifying grain boundary properties using sintering aids.[30] Aided by these recent advancements, the CCD has been reported to reach ≈1 mA cm^{-2}.[31–34] Despite the significant efforts laid toward understanding and mitigating the growth of filaments in LLZO, to date, its electro-chemo-mechanical origin is yet to be revealed. In fact, a number of studies have shown that electro-chemo-mechanical coupling

strongly affects the interfacial stability of solid-state batteries (SSBs).[35,36] One the one hand, local strain influences the interfacial contact and the electrochemical reaction rates. On the other hand, the electrochemical deposition of lithium can further cause mechanical deformation at the interfaces, forming a feedback loop. While there are indeed pioneer works from the theoreticians, the exact experimental measurement is still difficult. How the mechanical response and electrochemical performance correlates is yet to be answered.[37–40] Especially, since the stress is generated locally during lithium deposition, its characteristic effective length may well go down to nanometers. This leads to difficulty in direct measurements using conventional macroscopic electrochemical setups as shown in **Figure 1**a,b. They lack the spatial resolution to directly measure the triggering conditions and growth kinetics of an individual filament due to its small size as illustrated in Figure 1c. A direct example where local electro-chemo-mechanical coupling plays a critical role is the dendrite penetration at grain boundaries. It has been argued that Li filament prefers to penetrate the grain boundaries instead of grain interiors.[18] However, under what conditions such preferential nucleation happens and how they can be quantified still remains to be answered. In addition, the nanoscopic driving force of such inhomogeneity is still unresolved. Understanding such nanoscale interactions is also critical for the design of interface layers and prevention of filament growth.

In this work, we develop a high-resolution in situ characterization technique to probe the local dynamics and the electromechanical origin of lithium filament penetration, and use it as a guiding tool to design a highly efficient interphase to prevent short circuit and to achieve stable deposition. We exploit the extreme spatial resolution of conductive-atomic force microscopy (c-AFM) and utilize the AFM tip as the working electrode to selectively trigger dendrites in LLZO as illustrated in Figure 1d. By applying electric biases on the tip of the c-AFM,

we quantitatively measure the electrochemical responses of the lithium plating processes and the filament growth kinetics with the resolution down to nanometers. In particular, the intrinsically different responses of grain interior and grain boundaries to electrochemical lithium deposition are revealed for the first time. We find that the critical electrical bias to induce lithium filament growth at the grain boundary is ≈1/100 of that in the grain interior, as shown in Figure 1e. Such a striking difference points to the fact that the nanoscale inhomogeneity of the LLZO surface results in weak spots which enables a preferential penetration pathway for lithium metal. Further ex situ nanoelectro-mechanical AFM characterizations and finite element simulations suggest that the detouring and concentration of Li$^+$ flux at the interface between Li and LLZO grain boundaries is the major contributor that triggers penetration of the Li filament. Built on this understanding, we strategically adopted a highly efficient filament-proof interphase based on poly(propylene carbonate) (PPC) that is able to homogenize the local Li$^+$ flux and increase the CCD. Such an interphase in situ reacts with lithium metal at mild conditions and forms a highly conformal interface. The interfacial resistance drops from ≈1000 Ω cm^2 to an exceedingly low 14 Ω cm^2. The CCD value also increases from ≈0.2 to 1.8 mA cm^{-2} which is very close to the requirement of SSBs under practical conditions. Full SSLMBs are demonstrated using LiFePO$_4$ (LFP) and LiNi$_{0.5}$Co$_{0.2}$Mn$_{0.3}$O$_2$(NCM523) as cathodes. Apart from the application in SSBs, we also discover signature memristive switching characteristics of filaments in LLZO under cyclic conditions, which is essential in neuromorphic computing and nonvolatile memory devices.[41,42] A model memristor is designed and demonstrated based on the nanoelectrode with unprecedented stability of over 200 cycles and an on/off ratio of up to 10^5. The novel characterization technique developed in this work not only facilitates the understanding and the design of highly efficient interfaces that can potentially unlock the capabilities of SSLMBs, but also opens up new opportunities for solid electrolytes beyond energy applications.[41,42]

2. Results and Discussions

The experimental setup for the nanoelectrochemical characterizations is shown in Figure 1d. The c-AFM tip is used as the working electrode (WE) whereas Li metal functions as both the counter (CE) and the reference electrode (RE). The working principle of the system is illustrated in Figure S1 in the Supporting Information and explained in detail in the Supporting Information. By applying a reductive bias on the WE (i.e., negative with respect to Li/Li$^+$), the Li$^+$ ions are drawn from the LLZO to the tip of the c-AFM and are reduced to form lithium metal (Li^0). In principle, when the bias is small, the current is solely contributed by the flow of Li$^+$ ions and can be used as a proxy for the deposition rate of lithium metal. When the electric bias gets large enough, the lithium metal can penetrate through the LLZO pellet causing short circuits. Under such circumstances, the measured current goes through an abrupt change, indicating the transition from ionic to electronic conduction. In this study, we aim to monitor the electrochemical conditions (i.e., the bias and the current density) at which this tran-

sition happens. We use this value, i.e., the triggering bias, as the major proxy to quantify how easy it is for lithium filaments to penetrate LLZO as illustrated in Figure 1e and Figure S1 in the Supporting Information. In particular, for polycrystalline SEs such as LLZO, we focus on understanding how the grain interior differs from the grain boundaries as the latter has been speculated to be a weak spot for the penetration of Li, while actual quantitative electrochemical measurements have not been reported. The typical electrochemical results of a grain boundary are shown in Figure 1e. The current does not show significant increase until the bias is larger than −0.12 V versus Li/Li$^+$ where a surge in the conductivity is detected. Such a surge agrees with the metallic filament penetration and is supported by a back scan where an almost perfect linear relation between the current and the voltage is observed, indicating its pure Ohmic nature, as shown in **Figure 2**c.[27,43] Further mapping of the morphology change and the corresponding conductivity also confirms such a result. As shown in Figure 2a,b, highly conductive bumps emerge after the nanoelectrochemical measurements. Such a result reveals the penetrative and conductive feature of the bumps and further refers us to the fact that these bumps are indeed lithium dendrites. In addition, in situ optical characterizations were carried out to directly show the formation process of these conductive species, see Figures S2–S4 in the Supporting Information and the Supporting Information Video. Unambiguously, these bumps are the penetrated lithium dendrites and the points of short circuits. In contrast, for grain interiors, despite the high number of trials, we were only able to induce the filament growth for very limited times and all of them are triggered by large biases. A typical case is shown in Figures 1e and 2d where penetration of the metallic filament happens at < −9 V versus Li/Li$^+$. Such an astonishing ≈100-fold increase in the triggering bias for filament penetration unambiguously points to the fact that the grain boundary acts as a weak spot in the electrolyte and it should be mitigated as much as possible. To further verify the statistical significance of our nanoscale measurements, we carried out multiple independent tests and gathered the statistics. As shown in Figure 2e,f and Figure S5 in the Supporting Information, as we varied the distance of the c-AFM electrode to the grain boundary and changed the area of the electrode, the filament triggering bias for grain interior is consistently larger than the grain boundary. Therefore, though LLZO can intrinsically block Li filaments, such filament-proof capability can only be unlocked when the interfacial nanoinhomogeneities are eliminated.

Considering the 100-fold weakening of the SE at the grain boundary against lithium penetration, we further explored its mechanical and the electrical origin and use it to guide the design of an efficient filament-proof interphase. **Figure 3**a–e shows the nanomechanical measurement of a typical LLZO surface. The mechanical stiffness is clearly lower at the grain boundaries compared with the grain interiors. In order to avoid the influence of the abrupt changes of surface morphology on the accuracy of elastic property measurement, we specifically chose a relatively flat area and show the results in Figure 3d,e. The decrease at the grain boundaries can be as high as 30% compared with the interior. This is further supported by sampling the moduli along the vertical lines to the
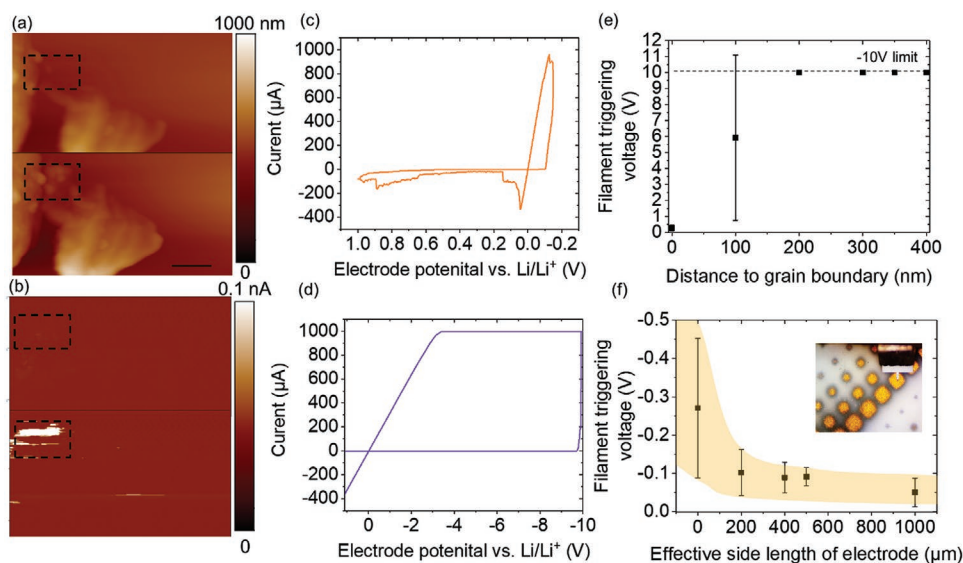
Figure 2. a) The morphology change of the LLZO surface before (upper panel) and after (lower panel) the penetration of lithium. b) The current map of the LLZO surface using c-AFM by applying a +0.1 V bias before (upper panel) and after (lower panel) the penetration of lithium. The scale bars in (a) and (b) are 200 nm. Typical current response of applying a cyclic bias at c) grain boundaries and d) grain interiors using the c-AFM nanoelectrode. The filament triggering bias measured e) with c-AFM tips at different distances to the grain boundaries and f) with deposited Au electrodes with different sizes. The inset in (f) shows the optical image of the deposited Au electrodes with different sizes.

grain boundaries, see Figure 3f and its inset. By averaging individual measurements, the moduli of LLZO decrease from ≈145 GPa in grain interiors to ≈120 GPa at grain boundaries. Such results are in good agreement with the simulations done by Yu and Siegel and show the statistical significance of the AFM measurements.[24] It is worthwhile to note that, despite the significant drop in the elastic moduli, the value is still significantly higher compared to that of Li metal. Therefore, the elastic softening should not be the sole factor that governs the filament growth. However, such mechanical inhomogeneity may serve as an initiator for the preferential lithium deposition and assists the Griffith-like crack extension mechanism proposed by Porz et al.[27] Beside the mechanical origin, the electronic aspects have also been speculated to affect the lithium deposition stability.[13,23,44–46] Here, we noticed that due to the electron insulating nature of LLZO, local inhomogeneity of electrical
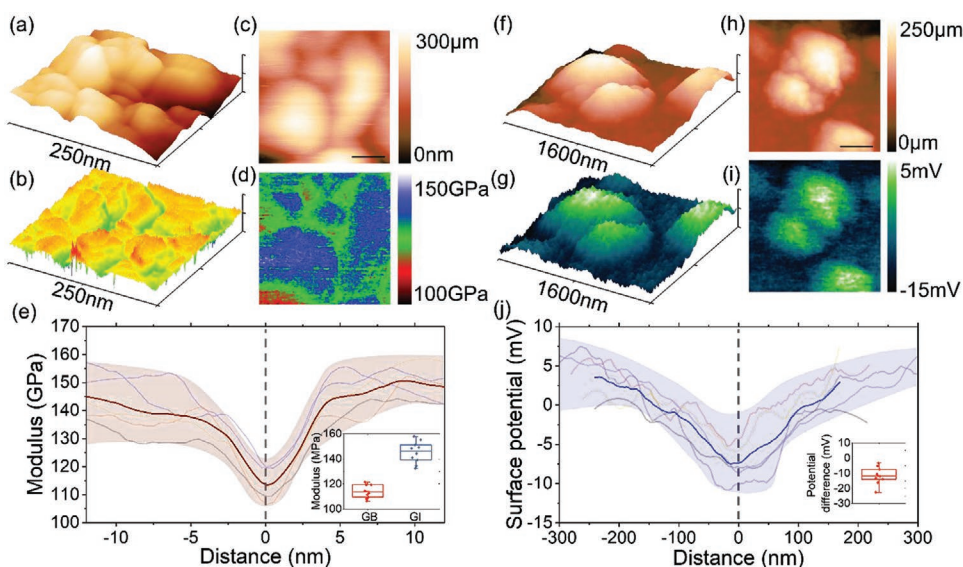
Figure 3. a) The morphology and b) the modulus mapping of the LLZO surfaces. (c) and (d) are the 2D view of selected areas. The scale bars in (c) and (d) are 50 nm. e) The local modulus as a function of the distance to the grain boundary. f) The morphology and g) the surface potential mapping of the LLZO surfaces. (c) and (d) are the corresponding 2D views. The scale bars in (c) and (d) are 500 nm. e) The surface potential as a function of the distance to the grain boundary. For (e) and (j), the brown and blue bold line in the foreground is the average of the results from five separate tests at diffract locations as indicated by the lines in the background. The shaded areas are guide to the eye to indicate the error range. The insets in (e) and (f) show the statistical data of the modulus and the surface potential at grain boundaries and at grain interiors.
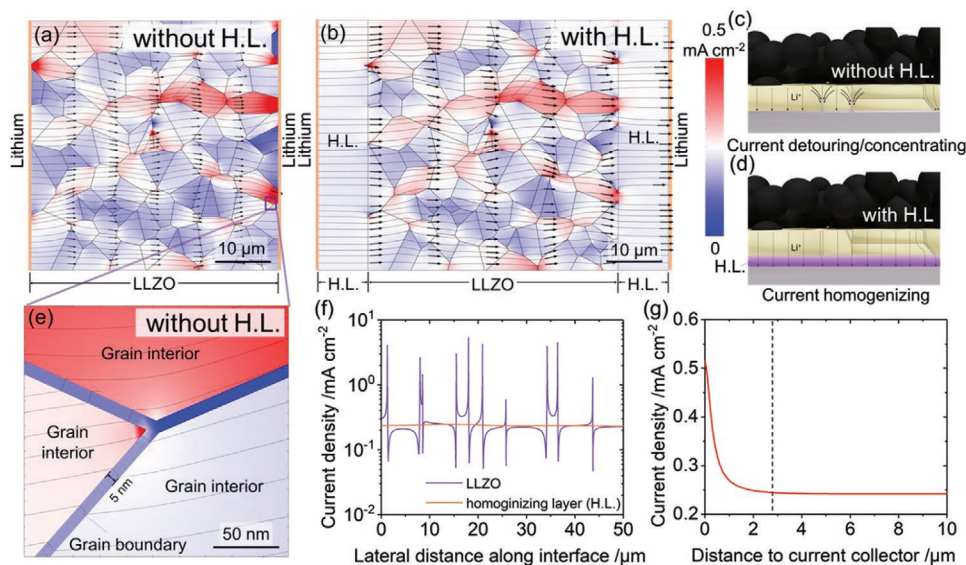
Figure 4. Simulated Li$^+$ flux distribution in a polycrystalline LLZO a) without and b) with HL. Illustration of c) the current detouring and concentrating at intrinsic Li|LLZO interfaces and d) the homogenizing effect at the HL-modified interfaces. e) Detailed Li$^+$ current density distribution at grain boundaries without HL. This is a zoomed image of the region highlighted with purple box in (a). f) The current density at Li|LLZO interfaces and the corresponding value after inserting HL. g) The maximum current density in HL with respect to the distance to the LLZO|HL interface.

potential may build up at the LLZO|electrode interfaces. Such variance of the electric local electric potential at the interface may give rise to nucleation preferences for lithium. In fact, at grain boundaries, it is known that certain charge-depleted or enriched region exist (also known as the space charge layer/space charge region).[47,48] We measure such local variance of electric potential by mapping the surface potential to the morphology using the Kelvin probe force microscopy.[49] The results are shown in Figure 3f–j. It is found that the surface potential of LLZO at grain boundaries tends to decrease by ≈10 mV compared with the grain interiors, see Figure 3j. Such a decrease corresponds to an e$^-$ accumulation or Li$^+$ depletion and is in agreement with a very recent MD simulation by Shiiba et al.[50] The decrease of Li$^+$ concentration may result in lowered conductivity and therefore a preference of lithium extrusion.[51,52] To study how the variation of local Li$^+$ diffusion could result in lithium penetration, we simulated the Li$^+$ flux in a polycrystalline LLZO with grain sizes on the order of ≈10 μm, see Figures S6 and S7 and Section S2 of the Supporting Information. As shown in **Figure 4**a–e, due to the low ionic conductivity of the grain boundaries, significant detour of Li$^+$ flux is observed. To minimize the probability of travelling through grain boundaries, Li$^+$ prefers to transport through certain grains instead of the others. This leads to strong spatial variation of current densities in LLZO and such inhomogeneity extends to the Li|LLZO interface. In fact, at the junction between Li and LLZO, the maximum current density within certain grains is over ten times larger than the others, as shown in Figure 4f. It is worthwhile to note that such a mechanism of current concentration would occur even under an ideal LLZO-Li contact. It is fundamentally different from the previously studied scenario, which involves imperfect contact due to limited interfacial wetting.[21] Essentially, in polycrystalline LLZO, even if the contact between LLZO and Li is perfect, "hot-spots" with high current densities

still exist. Therefore, to avoid such "hot-spots," an interlayer with homogenous ionic conductivity is necessary, as illustrated in Figure 4c,d. The effect of inserting such a homogenizing layer (HL) is simulated in Figure 4b where a grain boundary-free solid electrolyte with an ionic conductivity of 10^{-4} S cm^{-1} is attached between Li and LLZO. With such an interlayer, the Li$^+$ flux is effectively smoothened and the current density at the Li|HL interface shows almost no fluctuation as shown in Figure 4f. Interestingly, the homogenizing effect is relatively strong and the spike of current densities quickly drops to the average value when the HL is ≈3 μm thick. This value provides us with a guiding principle for the design of the interlayer.

Based on previous simulation results, an ideal HL is required to have the following characteristics: 1) It should display no spatial inhomogeneity in ionic conductivity. 2) The thickness should be on the order of μm and the ionic conductivity should be close to 10^{-4} S cm^{-1}. 3) It should be able to form good contact with both Li and LLZO and display small interfacial resistances. Considering these guidelines, we adopted a novel polymeric interphase based on PPC. We chose this material because it has been proposed as a solid electrolyte when combined with lithium salts and shows descent ionic conductivity.[53–55] More importantly, PPC goes through a catalytic de-polymerization reaction when heating together with Li.[56–58] Such a de-polymerization reaction can facilitate the contact between PPC and Li. Therefore, the handling of highly hazardous molten lithium is no longer necessary. In fact, PPC has already been reported as a superb buffer layer in both solid-state batteries and in liquid lithium metal batteries.[59–61] For example, Yang and co-workers used PPC between PEO and Li and observed better contact and slower interfacial degradation.[61] Yue et al. also reported similar results where they show PPC could enhance the compatibility of composite polymer electrolytes and Li.[62] In this work, we take a step further and show that, with the
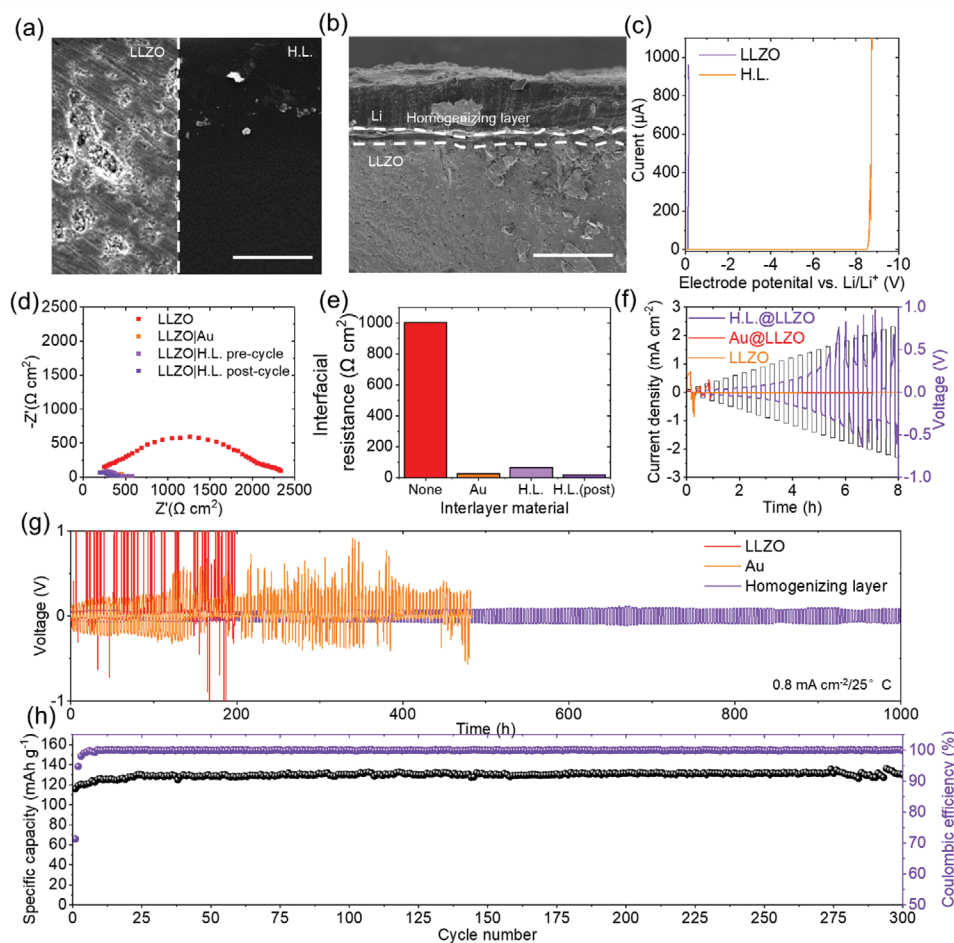
Figure 5. a) The morphology of polished LLZO surface and of HL. The scale bar in (a) is 50 µm. b) The cross-section of Li|HL|LLZO interfaces. The scale bar in (b) is 100 µm. c) The filament triggering bias on LLZO and HL. d) The electrochemical impedance spectroscopy of Li|LLZO|Li cells with no interlayers, Au interlayers, and HL. e) The interfacial resistance between Li and LLZO with different interlayers. f) The current density responses of Li|LLZO|Li cells with no interlayer, with Au interlayer, and with HL under increasing current densities. g) The current density responses of Li|LLZO|Li cells with no interlayer, with Au interlayer, and with HL under cyclic conditions at current density of 0.8 mA cm^{-2}. h) The specific capacity of SSBs using LFP as cathode under cyclic conditions.

unique property of PPC, it can serve as a superb interphasial layer to block dendrites in polycrystalline ceramic solid electrolytes via the homogenizing effect. **Figure 5**a,b and Figure S11 in the Supporting Information show morphological features of the HL. The HL covers the grain boundaries and other surface defects on LLZO, smoothing out the local variance. The electrochemical response of the two surfaces is shown in Figure 5c and Figure S11b in the Supporting Information. The filament triggering bias on the HL surface is not only significantly larger than that on LLZO (grain boundary regions), but is also homogenous throughout the entire region. The practical macroscopic electrochemical performance of the HL interphase is evaluated using Li|LLZO|Li coin cells. As shown in Figure 5d,e, the area resistance is ≈50 Ω cm^2 after inserting the PPC-based HL while the value for the intrinsic LLZO|Li interface without modification is ≈1000 Ω cm^2. Such a significant drop in impedance comes from the highly conformal interphase formed during the in situ de-polymerization process. Beyond that, ab initio molecular dynamics simulations show that the de-polymerization process creates molecular fragments and decreases the mole-

cular weight of the polymer, see Figures S13 and S14 in the Supporting Information. This explains the low interfacial resistance between PPC and LLZO.[58] In fact, a number of recent studies have shown that without any plasticizer, the interfacial resistance between solid-polymer electrolyte, e.g., polyethylene oxide and ceramics could be as high as ≈16 kΩ cm^2.[12,63,64] The inclusion of a loose-binding Li$^+$ solvent near the ceramic interface may facilitate Li$^+$ dissolution from the ceramic and therefore lead to a lower interfacial resistance.[65] Therefore, the superiority of PPC as an interfacial layer lies not only in its homogenous nature but also in its unique reaction mechanism with Li, which should be considered in future design of dendrite-proof interphases. Interestingly, we notice that after cycling the cell, the impedance decreases further to ≈14 Ω cm^2, such a value is even smaller than the pure inorganic Au|LLZO interface. This is probably because de-polymerization of PPC continued during cycling and further increased the conductivity of the interlayer, see Figures S8–S10 and Section S3 in the Supporting Information. Interestingly, a very recent report by Chen and co-workers gave similar results where they used PPC as an

interlayered for a different solid electrolyte.[59] The HL not only significantly reduces the interfacial resistance, but also enlarges the CCD, which is one of the major bottlenecks for practical SSBs. As shown in Figure 5f, the CCD for the intrinsic LLZO|Li case is <0.1 mA cm^{-2} while for the Au-modified case is ≈0.2 mA cm^{-2}. In comparison, in the HL-inserted case, the CCD reaches 1.8 mA cm^{-2}, almost ten times higher than the Au-modified case. Such a drastic increase in the capability of blocking filaments is in agreement with the simulation results and further confirms our strategy based on Li$^+$ flux homogenization is successful. To evaluate the sustainability of the interface, we performed long cyclic tests on Li symmetric cells and Li|SE|cathode full cells. The results are shown in Figure 5g,h and Figure S12 in the Supporting Information. At a high current density of 0.8 mA cm^{-2}, the HL-modified LLZO can stably withstand the electroplating and stripping of Li for over 1000 h. Full cells using our previously developed plasticized LFP and NCM523 composite electrodes also demonstrate superb cyclic stability.[66] Stable operation for more than 300 cycles is achieved.

Beyond the initial formation process, we also study the post-filament-penetration electrochemical kinetics of LLZO in hope of finding potential applications beyond SSBs. Interestingly, the formation of the metallic filament displays certain reversibility, i.e., when a reverse bias is applied, the metallic filament tends to be absorbed by the electrolyte and the short circuit is reversed. In fact, such a phenomenon has been observed in a number of recent work.[43,67,68] We take a step further and show that the filament growth in LLZO follows a memristive

behavior and the reversibility is highly dependent on the size of the electrode. Such memristive characteristics shares close resemblance with biological synapses and is the key to neuromorphic computing and nonvolatile memory, as illustrated in **Figure 6**a.[69] Figure 6b,c illustrates the typical I–V curve of a Li|LLZO|WE cell. When a negative bias (vs Li/Li$^+$) is applied, the Li$^+$ ions are drawn from LLZO toward the WE and are being reduced to form metallic Li as shown in Figure 6d. During this stage, the current is controlled by the ionic conduction of Li$^+$ and is not measurable with the current nanoelectrochemical measurement setup. This stage corresponds to the "off" state or the high-resistance-state (HRS) of an asymmetrical memristor. When the negative bias becomes larger, the lithium filament starts to grow and penetrates the LLZO pellet to form an electronically conductive path. Meanwhile, the nominal resistance becomes orders of magnitude higher. Such a transition corresponds to the "setting" of a memristor to its low-resistance-state (LRS) or the "on" state. Depending on the size of the electrode, the reversibility of such a process can be varied. As illustrated in the fourth panel of Figure 6d, if the size of the electrode is too large and the set bias is too high, the filament becomes too thick and the electrical potential is offset by the high electron conductivity and there is not enough driving force to strip Li away from the filament so as to break it for HRS. Therefore, the memristor fails. We prepared a number of WEs with different sizes as shown in the inset of Figure 2f. The Typical cyclic curves of the Li|LLZO|WE cells are shown in Figure 6e–g. In Figure 6e,
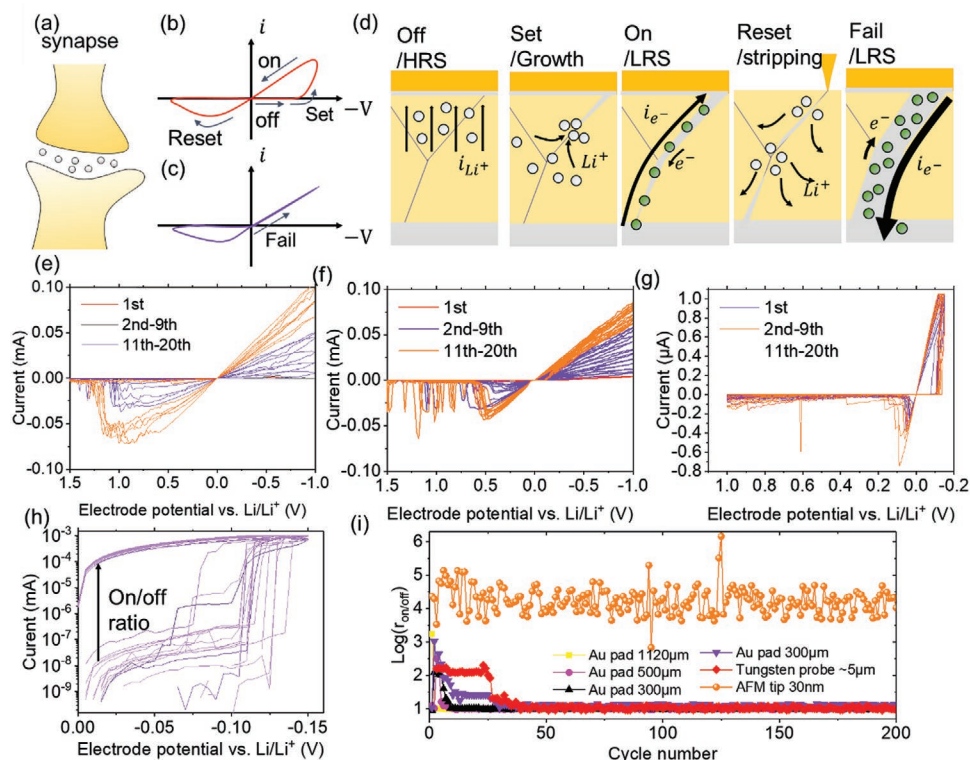
Figure 6. Illustration of a) a biological synapse and b,c) the typical response of a memristor. d) The corresponding internal physical processes with cyclic electric bias. I–V curves of Li|LLZO|WE memristors with WE being e) an Au pad with a 500 µm side length and f,g) an AFM tip. g) The I–V curve in log scale for (g). i) The variation of the on/off ratio with respect to cycle number for Li|LLZO|WE memristors with WE with different sizes. The set and reset potential limits are –0.2 and 1 V, respectively.

the side length of the WE is 500 µm which resembles the macroscopic scenario. During the initial cycle, we indeed observe the onset of the memristor. However, the ratio between the HRS and LRS state (the on/off ratio) is relatively small and did not go beyond 10. Also, after being "set" for the first time, it can hardly be "reset." This is in agreement with most macroscopic observations where the short circuit is detrimental to an SSB and can hardly be fully reversed.[70] However, when the size of the WEs shrinks to nanoscale, the reversibility becomes much better. Figure 6f shows the results of using the c-AFM tip as WE. The "set" bias stabilizes at ≈−0.25 V after several cycles and reset of the memristor is always successful. In fact, the on/off ratio within an operating voltage window of ±0.25 V kept almost constant after the first ten cycles. By limiting the set and reset voltages to −0.2 and +1 V, the memristive switching performance of the Li|LLZO|tip device is maximized. As shown in Figure 6g,h, extreme stability for over 200 cycles is achieved. Figure 6i gathers the cyclic stability of the on/off ratio versus electrode sizes. Only at nanoscale, stable memristive switching can be achieved. The memristor based on the nanoelectrode displays a rather high on/off ratio of 10^5 for 200 cycles. This may open up new opportunities for using lithium solid electrolytes in nonvolatile memory and neuromorphic computing, i.e., a new computing architecture beyond von Neumann,[69] and convert the notorious dendrite growth issue into something useful.

3. Conclusions

We develop an in situ nanoelectrochemical characterization technique based on c-AFM to reveal the nanoscopic origin of filament growth at the electrode–electrolyte interfaces in SSBs and use it to guide the design of a highly efficient filament-proof interphase. Significant nanoinhomogeneity of elastic modulus and Li^+ flux at the interfaces between polycrystalline LLZO and Li are identified as the major source of instability toward lithium penetration and short circuit. A highly conductive and conformal HL is designed to smooth out the nanoinhomogeneity and avoid the weak spots. A high CCD of 1.8 mA cm^{-2} and a low interfacial resistance of 14 Ohm cm^2 is achieved, approaching the practical requirement of SSBs. Full SSLMB cells are demonstrated using LFP and NCM523 as cathodes and show excellent stability for up to 300 cycles. Beyond energy applications, highly stable reversible memristive behavior of lithium filament is found at nanoscale. A model memristor with a high on/off ratio of 10^5 is demonstrated which can be cycled for over 200 times. The interfacial strategy proposed in the current work is highly efficient in preventing lithium filament growth in SSBs and may serve as a baseline for future design of interfaces for SSBs. The nanoelectrochemical characterization technique developed here not only provides insights into the nanoscopic electrochemical processes in SSBs but also opens up exciting opportunities for SEs beyond energy applications.

4. Experimental Section

Sample Preparation: The composition of the SE was $Li_{6.5}La_3Zr_{1.5}Ta_{0.5}O_{12}$, where the Ta doping helped stabilize the cubic phase. It was named

as LLZO throughout the article for simplicity despite the Ta dopant. The SE was synthesized via a conventional solid-state reaction where $LiOH \cdot H_2O$ (≥ 99.0%, Sigma-Aldrich), La_2O_3 (99%, Sigma-Aldrich), Ta_2O_5 (≥ 99.99%, Ourchem), and ZrO_2 (<100 nm, Sigma-Aldrich) were used as starting materials.[66] After weighing stoichiometric amount the starting materials with 10% Li-excess and wet ball-milling with isopropanol, the mixed power was dried and sintered at 900 °C in air for 12 h followed by pelletization with another 10 wt% $LiOH \cdot H_2O$ added. Finally, the green pellets were sintered at 1140 °C for 16 h in MgO crucibles which were covered with a lid. Mother powder was added on top of the pellet to minimize the Li loss. The prepared disks were then sanded down to the thickness of ≈300 µm. ≈50 nm thick Au was then deposited on one side of the pellet and a lithium foil was attached to the same side as the counter and the reference electrode followed by melting at 250 °C. This step ensured a good contact of the counter and the reference electrode.

AFM and Nanoelectrochemical Measurements: The topography and AFM current–voltage (*I–V*) curves were measured using an in-house developed c-AFM setup with a ==Benyuan system (CSPM5500, China)== in a glove box (O_2 and H_2O < 1 ppm) and with a Keithly 2400 sourcemeter as the electrochemical measurement unit. Pt probes with tip radius of 20 nm (25PT300B, Rocky Mountain nanotechnology, USA) were used for CP-AFM measurement. The modulus and scanning Kelvin probe microscopy (SKPM) measurements were performed with a Dimension Icon system (NANOSCOPE V7-B, Bruker, USA). The absolute value of the modulus was calibrated by matching the value of the grain interior to indentation results on LLZO grains.[71] Pt-coated Si probes with a tip radius of 20 nm (SCM-PIT-75, 75 kHz, 2.8 N m^{-1}) were used. Topography images and modulus images or SKPM images were taken simultaneously at a scan rate of 1 Hz. During the nanoelectrochemical measurements, the current was limited to 1 mA and the voltage to 10 V to avoid damage to the c-AFM tip.

Macroscopic Electrochemical Tests: The HL was fabricated by dissolving PPC (M_w = 50 000, Sigma-Aldrich) and lithium bis(trifluoromethane)-sulfonimide (LiTFSI, Sigma-Aldrich) with a weight ratio of 8:2 in *N,N*-dimethylformamide (Sigma-Aldrich) followed by coating the solution on LLZO pellets. The film was then vacuum dried at 80 °C for 24 h. After that, lithium foils were attached to both sides of HL-coated LLZO pellets and heated at 80 °C for 2 h. The CCDs were estimated by constant current measurement of Li|LLZO|Li cells with increasing current densities from 0 to 3 mA cm^{-2}. The tests were carried out at 25 °C. For comparison, the cells without any interlayer and with Au interlayer were fabricated similarly except that Li was melted on the pellet at 250 °C to achieve better contact. For the Au-coated case, ≈50 nm thick Au was deposited on LLZO. For full-cell tests, LFP and NCM523 cathodes were fabricated following previous work, by coating an *N*-methylpyrrolidone slurry containing the cathode powder, the poly(vinylidene fluoride) binder, conductive carbon, succinonitrile, and LiTFSI with a weight ratio of 5:1:1:2:1 on an LLZO pellet followed by vacuum drying at 80 °C for 24 h.[66] The charge and discharge tests of the LFP and the NCM523 cells were carried out by applying constant currents to the cells. The cutoff voltages were of 2.5–4.2 and 2.8–4.2 V, respectively. The testing temperatures were 40 °C for the LFP cell to achieve better rate-capability and larger cycle numbers. For NCM523 cells, the tests were carried out at 30 °C.

Ab Initio Molecular Dynamics Simulations: Ab initio molecular dynamics simulations were carried out using the CASTEP plane-wave density functional theory code.[72] The QC5 set of pseudopotential was used with a relatively low energy cutoff of 340 meV. The calculation was spin polarized. The brillouin zone was sampled on the gamma point. The temperature was controlled at 500 K using a Nosé–Hoover thermostat.[73] Such a temperature was chosen to speed up the simulation and to enhance sampling. The time step for the ionic motion was set to 1 fs. The simulation box was built by including a Li surface, a linear PPC with five molecular units, and a vacuum layer of 15 Å. The detailed model is shown in Figure S13 in the Supporting Information.

Finite Element Simulations: The Li^+ flux distribution in the solid electrolyte and the HL was simulated by solving the electrostatics in

a polycrystalline LLZO as detailed in Section S4 in the Supporting Information. The grain distribution was generated using a Voronoi tessellation.[74] The average size of each grain was ≈10 μm. The diameter of grain boundaries was set to 5 nm. The detailed geometry and the mesh used in the simulation are shown in Figure S15 in the Supporting Information. Constant potentials of 0.1 and 0 V were used as boundary conditions on the two sides of the electrolyte. The materials constants used in the simulation are listed in Table S1 in the Supporting Information. For the case of HL-coated LLZO, two HL with a thickness of 10 μm each were attached to both sides of the LLZO. Other parameters were kept the same.

Calculation of the Contact Area: The contact area between LLZO and the AFM-tip was calculated using the following relation derived from Herzian contact mechanics[75]

$$A = \pi \left(\frac{3 P_{eff}}{4 E^*} r \right)^{2/3} \tag{1}$$

where r is the tip radius, P_{eff} is the tip pressure force, and E^* is the effective modulus of LLZO.[76] The tip radius was about 20 nm and the tip pressure was about 400 nN calculated from our force curve measurement. From this calculation, the contact area in these studies were assessed to be ≈30 nm².

Supporting Information

Supporting Information is available from the Wiley Online Library or from the author.

Acknowledgements

Conflict of Interest

The authors declare no conflict of interest.

Data Availability Statement

Research data are not shared.

Keywords

[1] J. W. Choi, D. Aurbach, *Nat. Rev. Mater.* **2016**, *1*, 16013.
[2] D. Lin, Y. Liu, Y. Cui, *Nat. Nanotechnol.* **2017**, *12*, 194.
[3] B. Han, D. Xu, S. S. Chi, D. He, Z. Zhang, L. Du, M. Gu, C. Wang, H. Meng, K. Xu, *Adv. Mater.* **2020**, *32*, 2004793.
[4] Q. Pang, X. Liang, C. Y. Kwok, L. F. Nazar, *Nat. Energy* **2016**, *1*, 16132.
[5] J. Liu, Z. Bao, Y. Cui, E. J. Dufek, J. B. Goodenough, P. Khalifah, Q. Li, B. Y. Liaw, P. Liu, A. Manthiram, *Nat. Energy* **2019**, *4*, 180.
[6] Z. Yu, H. Wang, X. Kong, W. Huang, Y. Tsao, D. G. Mackanic, K. Wang, X. Wang, W. Huang, S. Choudhury, *Nat. Energy* **2020**, *5*, 526.
[7] S. Chen, J. Zheng, D. Mei, K. S. Han, M. H. Engelhard, W. Zhao, W. Xu, J. Liu, J. G. Zhang, *Adv. Mater.* **2018**, *30*, 1706102.
[8] D. Kang, N. Hart, J. Koh, L. Ma, W. Liang, J. Xu, S. Sardar, J. P. Lemmon, *Energy Storage Mater.* **2020**, *24*, 618.
[9] Q. Yang, W. Li, C. Dong, Y. Ma, Y. Yin, Q. Wu, Z. Xu, W. Ma, C. Fan, K. Sun, *J. Energy Chem.* **2020**, *42*, 83.
[10] J. Yi, J. Chen, Z. Yang, Y. Dai, W. Li, J. Cui, F. Ciucci, Z. Lu, C. Yang, *Adv. Energy Mater.* **2019**, *9*, 1901796.
[11] J. Janek, W. G. Zeier, *Nat. Energy* **2016**, *1*, 16141.
[12] Z. Zou, Y. Li, Z. Lu, D. Wang, Y. Cui, B. Guo, Y. Li, X. Liang, J. Feng, H. Li, *Chem. Rev.* **2020**, *120*, 4169.
[13] H. Liu, X.-B. Cheng, J.-Q. Huang, H. Yuan, Y. Lu, C. Yan, G.-L. Zhu, R. Xu, C.-Z. Zhao, L.-P. Hou, *ACS Energy Lett.* **2020**, *5*, 833.
[14] R. Murugan, V. Thangadurai, W. Weppner, *Angew. Chem., Int. Ed.* **2007**, *46*, 7778.
[15] N. Zhao, W. Khokhar, Z. Bi, C. Shi, X. Guo, L.-Z. Fan, C.-W. Nan, *Joule* **2019**, *3*, 1190.
[16] C. Wang, K. Fu, S. P. Kammampata, D. W. McOwen, A. J. Samson, L. Zhang, G. T. Hitz, A. M. Nolan, E. D. Wachsman, Y. Mo, *Chem. Rev.* **2020**, *120*, 4257.
[17] C. Monroe, J. Newman, *J. Electrochem. Soc.* **2005**, *152*, A396.
[18] Y. Ren, Y. Shen, Y. Lin, C.-W. Nan, *Electrochem. Commun.* **2015**, *57*, 27.
[19] X. Han, Y. Gong, K. K. Fu, X. He, G. T. Hitz, J. Dai, A. Pearse, B. Liu, H. Wang, G. Rubloff, Y. Mo, V. Thangadurai, E. D. Wachsman, L. Hu, *Nat. Mater.* **2017**, *16*, 572.
[20] C. Wang, Y. Gong, B. Liu, K. Fu, Y. Yao, E. Hitz, Y. Li, J. Dai, S. Xu, W. Luo, E. D. Wachsman, L. Hu, *Nano Lett.* **2017**, *17*, 565.
[21] A. Sharafi, E. Kazyak, A. L. Davis, S. Yu, T. Thompson, D. J. Siegel, N. P. Dasgupta, J. Sakamoto, *Chem. Mater.* **2017**, *29*, 7961.
[22] A. Sharafi, H. M. Meyer, J. Nanda, J. Wolfenstine, J. Sakamoto, *J. Power Sources* **2016**, *302*, 135.
[23] F. Han, A. S. Westover, J. Yue, X. Fan, F. Wang, M. Chi, D. N. Leonard, N. J. Dudney, H. Wang, C. Wang, *Nat. Energy* **2019**, *4*, 187.
[24] S. Yu, D. J. Siegel, *ACS Appl. Mater. Interfaces* **2018**, *10*, 38151.
[25] P. Barai, K. Higa, A. T. Ngo, L. A. Curtiss, V. Srinivasan, *J. Electrochem. Soc.* **2019**, *166*, A1752.
[26] J. F. Nonemacher, G. Arinicheva, G. Yan, M. Finsterbusch, M. Krüger, J. Malzbender, *J. Eur. Ceram. Soc.* **2020**, *40*, 3057.
[27] L. Porz, T. Swamy, B. W. Sheldon, D. Rettenwander, T. Frömling, H. L. Thaman, S. Berendts, R. Uecker, W. C. Carter, Y. M. Chiang, *Adv. Energy Mater.* **2017**, *7*, 1701003.
[28] J. Wen, Y. Huang, J. Duan, Y. Wu, W. Luo, L. Zhou, C. Hu, L. Huang, X. Zheng, W. Yang, *ACS Nano* **2019**, *13*, 14549.
[29] X. Fu, T. Wang, W. Shen, M. Jiang, Y. Wang, Q. Dai, D. Wang, Z. Qiu, Y. Zhang, K. Deng, *Adv. Mater.* **2020**, *32*, 2000575.
[30] B. Xu, W. Li, H. Duan, H. Wang, Y. Guo, H. Li, H. Liu, *J. Power Sources* **2017**, *354*, 68.
[31] H. Huo, Y. Chen, R. Li, N. Zhao, J. Luo, J. G. P. da Silva, R. Mücke, P. Kaghazchi, X. Guo, X. Sun, *Energy Environ. Sci.* **2020**, *13*, 127.
[32] H. Huo, J. Liang, N. Zhao, X. Li, X. Lin, Y. Zhao, K. Adair, R. Li, X. Guo, X. Sun, *ACS Energy Lett.* **2020**, *5*, 2156.
[33] W. Feng, X. Dong, X. Zhang, Z. Lai, P. Li, C. Wang, Y. Wang, Y. Xia, *Angew. Chem., Int. Ed.* **2020**, *59*, 5346.
[34] J. Meng, Y. Zhang, X. Zhou, M. Lei, C. Li, *Nat. Commun.* **2020**, *11*, 1.
[35] P. Wang, W. Qu, W. L. Song, H. Chen, R. Chen, D. Fang, *Adv. Funct. Mater.* **2019**, *29*, 1900950.
[36] R. Raj, J. Wolfenstine, *J. Power Sources* **2017**, *343*, 119.

**ADVANCED
SCIENCE NEWS**

www.advancedsciencenews.com

**ADVANCED
ENERGY
MATERIALS**

www.advenergymat.de

[37] Y. Tang, L. Zhang, J. Chen, H. Sun, T. Yang, Q. Liu, Q. Huang, T. Zhu, J. Huang, *Energy Environ. Sci.* **2021**, *14*, 602.

[38] T. H. Wan, F. Ciucci, *Electrochim. Acta* **2020**, *331*, 135355.

[39] Q. Liu, L. Zhang, H. Sun, L. Geng, Y. Li, Y. Tang, P. Jia, Z. Wang, Q. Dai, T. Shen, *ACS Energy Lett.* **2020**, *5*, 2546.

[40] L. Zhang, T. Yang, C. Du, Q. Liu, Y. Tang, J. Zhao, B. Wang, T. Chen, Y. Sun, P. Jia, *Nat. Nanotechnol.* **2020**, *15*, 94.

[41] J. J. Yang, D. B. Strukov, D. R. Stewart, *Nat. Nanotechnol.* **2013**, *8*, 13.

[42] Q. Xia, J. J. Yang, *Nat. Mater.* **2019**, *18*, 309.

[43] T. Krauskopf, R. Dippel, H. Hartmann, K. Peppler, B. Mogwitz, F. H. Richter, W. G. Zeier, J. Janek, *Joule* **2019**, *3*, 2030.

[44] Y. Song, L. Yang, W. Zhao, Z. Wang, Y. Zhao, Z. Wang, Q. Zhao, H. Liu, F. Pan, *Adv. Energy Mater.* **2019**, *9*, 1900671.

[45] Y. Song, L. Yang, L. Tao, Q. Zhao, Z. Wang, Y. Cui, H. Liu, Y. Lin, F. Pan, *J. Mater. Chem. A* **2019**, *7*, 22898.

[46] H.-K. Tian, B. Xu, Y. Qi, *J. Power Sources* **2018**, *392*, 79.

[47] J.-F. Wu, X. Guo, *Phys. Chem. Chem. Phys.* **2017**, *19*, 5880.

[48] N. Goswami, R. Kant, *J. Electroanal. Chem.* **2019**, *835*, 227.

[49] M. Nonnenmacher, M. o'Boyle, H. K. Wickramasinghe, *Appl. Phys. Lett.* **1991**, *58*, 2921.

[50] H. Shiiba, N. Zettsu, M. Yamashita, H. Onodera, R. Jalem, M. Nakayama, K. Teshima, *J. Phys. Chem. C* **2018**, *122*, 21755.

[51] S. Yu, D. J. Siegel, *Chem. Mater.* **2017**, *29*, 9639.

[52] W. Li, S. Cohen, K. Gartsman, R. Caballero, P. Van Huth, R. Popovitz-Biro, D. Cahen, *Sol. Energy Mater. Sol. Cells* **2012**, *98*, 78.

[53] J. Zhang, J. Zhao, L. Yue, Q. Wang, J. Chai, Z. Liu, X. Zhou, H. Li, Y. Guo, G. Cui, *Adv. Energy Mater.* **2015**, *5*, 1501082.

[54] J. Zhang, X. Zang, H. Wen, T. Dong, J. Chai, Y. Li, B. Chen, J. Zhao, S. Dong, J. Ma, *J. Mater. Chem. A* **2017**, *5*, 4940.

[55] Y. Li, F. Ding, Z. Xu, L. Sang, L. Ren, W. Ni, X. Liu, *J. Power Sources* **2018**, *397*, 95.

[56] B. Commarieu, A. Paolella, S. Collin-Martin, C. Gagnon, A. Vijh, A. Guerfi, K. Zaghib, *J. Power Sources* **2019**, *436*, 226852.

[57] M.-X. Jing, H. Yang, H. Chen, S. Hua, B.-W. Ju, Q. Zhou, F.-Y. Tu, X.-Q. Shen, S.-B. Qin, *SN Appl. Sci.* **2019**, *1*, 205.

[58] C. Wang, H. Zhang, J. Li, J. Chai, S. Dong, G. Cui, *J. Power Sources* **2018**, *397*, 157.

[59] Y. Chen, W. Li, C. Sun, J. Jin, Q. Wang, X. Chen, W. Zha, Z. Wen, *Adv. Energy Mater.* **2020**, *11*, 2002545.

[60] Q. Yu, W. Mai, W. Xue, G. Xu, Q. Liu, K. Zeng, Y. Liu, F. Kang, B. Li, J. Li, *ACS Appl. Mater. Interfaces* **2020**, *12*, 27087.

[61] H. Yang, Y. Zhang, M. J. Tennenbaum, Z. Althouse, Y. Ma, Y. He, Y. Wu, T.-H. Wu, A. Mathur, P. Chen, *ACS Appl. Mater. Interfaces* **2019**, *11*, 27906.

[62] H. Yue, J. Li, Q. Wang, C. Li, J. Zhang, Q. Li, X. Li, H. Zhang, S. Yang, *ACS Sustainable Chem. Eng.* **2018**, *6*, 268.

[63] D. Brogioli, F. Langer, R. Kun, F. La Mantia, *ACS Appl. Mater. Interfaces* **2019**, *11*, 11999.

[64] A. Gupta, J. Sakamoto, *Electrochem. Soc. Interface* **2019**, *28*, 63.

[65] X. C. Chen, X. Liu, A. Samuthira Pandian, K. Lou, F. M. Delnick, N. J. Dudney, *ACS Energy Lett.* **2019**, *4*, 1080.

[66] Z. Lu, J. Yu, J. Wu, M. B. Effat, S. C. Kwok, Y. Lyu, M. M. Yuen, F. Ciucci, *Energy Storage Mater.* **2019**, *18*, 311.

[67] C. Wang, Y. Gong, J. Dai, L. Zhang, H. Xie, G. Pastel, B. Liu, E. Wachsman, H. Wang, L. Hu, *J. Am. Chem. Soc.* **2017**, *139*, 14257.

[68] W. Ping, C. Wang, Z. Lin, E. Hitz, C. Yang, H. Wang, L. Hu, *Adv. Energy Mater.* **2020**, *10*, 2000702.

[69] Z. Wang, S. Joshi, S. E. Savel'ev, H. Jiang, R. Midya, P. Lin, M. Hu, N. Ge, J. P. Strachan, Z. Li, *Nat. Mater.* **2017**, *16*, 101.

[70] D. Cao, X. Sun, Q. Li, A. Natan, P. Xiang, H. Zhu, *Matter* **2020**, *3*, 57.

[71] J. E. Ni, E. D. Case, J. S. Sakamoto, E. Rangasamy, J. B. Wolfenstine, *J. Mater. Sci.* **2012**, *47*, 7978.

[72] M. Segall, P. J. Lindan, M. a. Probert, C. J. Pickard, P. J. Hasnip, S. Clark, M. Payne, *J. Phys.: Condens. Matter* **2002**, *14*, 2717.

[73] D. J. Evans, B. L. Holian, *J. Chem. Phys.* **1985**, *83*, 4069.

[74] Q. Du, V. Faber, M. Gunzburger, *SIAM Rev.* **1999**, *41*, 637.

[75] V. B. Engelkes, J. M. Beebe, C. D. Frisbie, *J. Phys. Chem. B* **2005**, *109*, 16801.

[76] S. Yu, R. D. Schmidt, R. Garcia-Mendez, E. Herbert, N. J. Dudney, J. B. Wolfenstine, J. Sakamoto, D. J. Siegel, *Chem. Mater.* **2016**, *28*, 197.